A capillary specimen aberration for describing X-ray powder diffraction line profiles for convergent, divergent and parallel beam geometries

Alan A. Coelho and Matthew R. Rowles

A capillary specimen aberration for describing X-ray powder diffraction line profiles for convergent, divergent and parallel beam geometries

Alan A. Coelho[a]* and Matthew R. Rowles[b]

[a]72 Cedar Street, Wynnum, Brisbane, Queensland 4178, Australia, and [b]Department of Physics and Astronomy, Curtin University, Australia. *Correspondence e-mail: alancoelho@bigpond.com

X-ray powder diffraction patterns of cylindrical capillary specimens have substantially different peak positions, shapes and intensities relative to patterns from flat specimens. These aberrations vary in a complex manner with diffraction angle and instrument geometry. This paper describes a fast numerical procedure that accurately describes the capillary aberration in the equatorial plane for convergent focusing, divergent and parallel beam instrument geometries. Axial divergence effects are ignored and only a cross section of the capillary, a disc, is considered; it is assumed that axial divergence effects can be described using an additional correction that is independent of the disc correction. Significantly, the present implementation uses the *TOPAS-Academic* aberration approximation technique of averaging nearby aberrations in 2θ space to approximate in-between aberrations, which results in no more than $\sim$30 disc aberrations calculated over the entire 2θ range, even when the diffraction pattern comprises thousands of peaks. Finally, the disc aberration is convoluted with the emission profile and other instrument and specimen aberrations in a Rietveld refinement sense, allowing for refinement on the specimen's absorption coefficient and capillary diameter, as well as the instrument focal length. Large differences between refined and expected values give insight into instrument alignment.

1. Introduction

Diffraction peak positions and intensities collected from a capillary specimen in parallel beam geometry are typically corrected using an analytical function (Sabine *et al.*, 1998). Correcting for peak shapes, however, has not previously been performed, most probably because of its complexity and the estimated large computing power necessary. Nevertheless, with careful numerical procedures, the peak shapes can be accurately described with a small amount of computation. We first define the two instrument geometries of convergent and divergent beam geometries as seen in Fig. 1. Parallel beam geometry can be thought of as being a case of an infinite focal length. For the case of capillaries illuminated with an X-ray beam short in length in the axial plane, the specimen can be considered a disc centred on the diffractometer axis with consideration given only to the equatorial plane (Sulyanov *et al.*, 2012). It is assumed that the intensity distribution of the incident beam is uniform and that the entire disc is bathed in X-rays. The peak shape aberration along the length of the capillary in the axial plane can then be further described using an axial divergence aberration (Cheary & Coelho, 1998) and is not considered here.

The intensity contribution from the whole disc has been determined numerically by Dwiggins (1972, 1975); however,
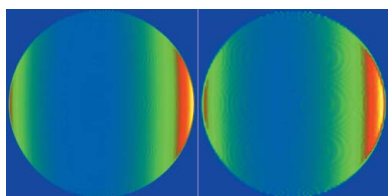
the objective here is not only to determine intensity contributions but to additionally determine the shape of the aberration. The formation of the disc aberration can be broken down into three steps (Fig. 1): (i) calculation of diffraction intensities along lines parallel to the diffracting vector (along the x axis) for $x > 0$ and separately for $x < 0$; (ii) summing the line aberrations into a single aberration ensuring the centroid and intensity of the aberration are accurate; and (iii) applying a smoothing function to smooth out ripples caused by the discrete nature of the process. From symmetry, a line aberration calculated at y is a good approximation to the aberration at $-y$, but shifted along the 2θ axis.

2. Diffracting intensities from a line on the disc parallel to the x axis

The following development of the disc aberration applies to both convergent and divergent beam geometries (Fig. 1). In
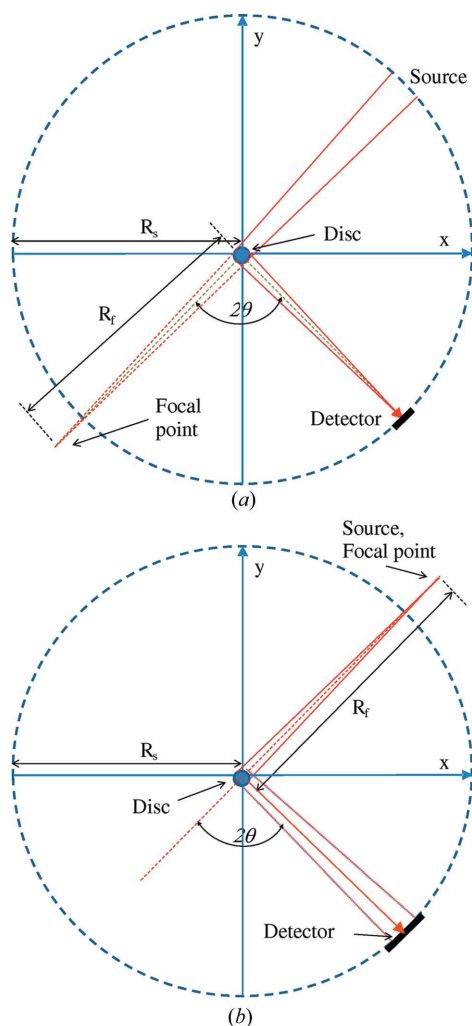

(a)

(b)

Figure 1
(a) Convergent and (b) divergent beam geometries. R_s = diffractometer radius, R_f = focal length. With the origin at the centre of the disc, the detector moves along the diffractometer circle from $(R_s, 0)$ to $(0, -R_s)$ and the source moves from $(0, R_s)$ to $(R_s, 0)$. Both the source and detector move such that a source position (x, y) corresponds to a detector position $(x, -y)$.

both cases, the measured 2θ positions are determined with the focal point considered as the source of the rays. All analyses are performed using the *TOPAS-Academic* software (Coelho, 2017).

We first consider the aberration arising from a line on the disc parallel to the x axis for $x > 0$, which we will call line-on-disc (see Fig. 2). The intensity contribution from the line is given by equation (1), where r is the radius of the disc, μ is the linear absorption coefficient of the material taking into account its packing density and $P(x, y, 2\theta)$ is the path length through the disc at x for a Bragg angle of 2θ:

$$I(y, 2\theta) = \int_0^{r_y} \exp[-\mu P(x, y, 2\theta)]\, dx, \quad \text{where} \quad r_y = (r^2 - y^2)^{1/2}.$$

(1)

The intensity contribution from the line does not determine where on the 2θ axis the intensity should be placed in order to form the aberration. The line is therefore broken into segments and the intensity contribution from each segment transformed on to the corresponding 2θ axis of the diffraction pattern. Too few segments along the line will produce inaccurate aberration shapes and intensities. The integral of equation (1) for $I(x, y)$ can be efficiently evaluated numerically by choosing values of x that vary as a function of μ such that the variation of $P(x, y, 2\theta)$ within a particular segment can be considered linear. The resulting integral at one of the discrete points, x_j, at the midpoint of a segment is

$$I(x_j, y, 2\theta) = \int_{x_{1,j}}^{x_{2,j}} \exp[-\mu(m_j x + c_j)]\, dx,$$

$$\text{where} \quad x_{1,j} = \tfrac{1}{2}(x_{j-1} + x_j), \quad x_{2,j} = \tfrac{1}{2}(x_{j+1} + x_j),$$

$$m_j = \frac{P(x_{2,j}, y, 2\theta) - P(x_{1,j}, y, 2\theta)}{x_{2,j} - x_{1,j}},$$

$$c_j = P(x_{2,j}, y, 2\theta) - m_j x_{2,j}.$$

(2)

For accuracy, $I(x_j, y, 2\theta)$ for each x_j should be equal, or $I(x_{j+1}, y, 2\theta) = I(x_j, y, 2\theta)$. This condition can be met by setting $P(x_{j+1}, y, 2\theta) - P(x_j, y, 2\theta) = c$, where c is some chosen change in path length. For $2\theta = 180°$ and for $y = 0$, this condition can be met exactly by solving for x_j in equation (3):
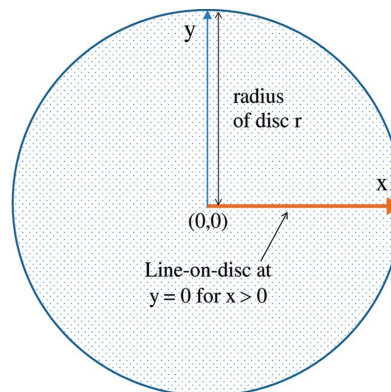

Figure 2
Schematic of the disc and the line-on-disc with the origin at the centre of the disc.

$$I(x_j, 0, 90) = \int_{x_{1,j}}^{x_{2,j}} \exp[-\mu(r_y - x)]\,dx = \Delta A,$$

$$\text{where} \quad \Delta A = \frac{A}{N_y} = \frac{1}{N_y} \int_0^{r_y} \exp(-\mu x)\,dx \qquad (3)$$

$$= [1 - \exp(-\mu r_y)]\frac{1}{\mu N_y}.$$

Or, $x_j = r_y + \ln(1 - j\mu\Delta A)/\mu$, where N_y corresponds to the number of chosen x_j points and A is the total intensity along the line-on-disc at $y = 0$. For $2\theta < 180°$, equation (2) needs to be equated to ΔA and then solved numerically for x_j. The positions of x_j for various 2θ are shown by the markers (circles) in Fig. 3. These path-length curves are independent of μ; however, the positions of the x_j points are dependent on μ. As can be seen, a linear approximation of path length becomes less accurate as 2θ decreases, leading to inaccurate $I(x_j, 0, 2\theta)$ values. Solving equation (2) for x_j numerically for $2\theta < 180°$ is computationally expensive and serves only to place x_j such that $I(x_{j+1}, 0, 2\theta) = I(x_j, 0, 2\theta)$ for all j. To approximately do the same, equation (3) can be used for all 2θ with additional points added for low 2θ. These additional points can be added by compressing the x axis; preliminary analysis has shown that multiplying the x axis by $q = \frac{1}{2}[1 + \sin(\theta)]$ works well, as described in equation (4):

$$\int_{x_{1,j}}^{x_{2,j}} \exp[-\mu(r_y - qx)]\,dx = \Delta A \qquad (4)$$

$$\text{or} \quad x_j = r_y + \ln(1 - j\mu q\Delta A)/(\mu q).$$

Additionally, for $y \neq 0$, the path length *versus* x curves, similar to Fig. 3, have an excess of points with increasing y. In this case, some x_j points are removed by expanding the x axis by dividing the step size in x_j by r_y/r, resulting in the final x_j determination equation of

$$x_j = r_y + \ln(1 - j\mu q\Delta A)r/(\mu q r_y). \qquad (5)$$

Equation (5) concentrates the x_j points towards the edge of the disc for high-absorbing materials and more evenly across the disc for low-absorbing materials; this is shown for various 2θ and μ in Fig. 4. Also shown is the increase in the number of points for low 2θ values as μ increases.

At small 2θ angles, rays passing close to the left edge of the disc can contribute in a nontrivial manner. Thus, x_j values should also occur more frequently as x approaches $-r_y$. This is achieved by setting the x_j values for $x_j < 0$ to the negative of the x_j values for $x_j > 0$. Thus, stepping along a line parallel to the x axis is performed as follows:

(1) Calculate $I(x_j, y)$ for $x_j > 0$ starting with $x_{2,j}$ at r_y.

(2) Calculate $I(-x_j, y)$ for $x_j < 0$ starting with $x_{1,j}$ at $-r_y$.

For case (1) the path length through the specimen for a ray diffracting at x, for $x > 0$, is greater than that for $x + \Delta$, where Δ is some positive value, that is, $I(x_j, y)$ is always less than $I(x_j + \Delta, y)$. Thus, calculation of $I(x_j, y)$ can be terminated after the intensity drops off to a sufficiently small value, $t = 10^{-4}$, or calculation is terminated when $\exp[-\mu P(x_j, 2\theta)] < t$. For case (2) and starting at $x = -r$ the path length is more complicated as x increases; it is also a function of 2θ, as seen in Fig. 3. However, the path length is always greater at either $x = -r$ or $x = 0$. Termination of the calculation can therefore occur when both $\exp[-\mu P(x_j, 2\theta)] < t$ and $\exp[-\mu P(x_j = 0, 2\theta)] < t$.
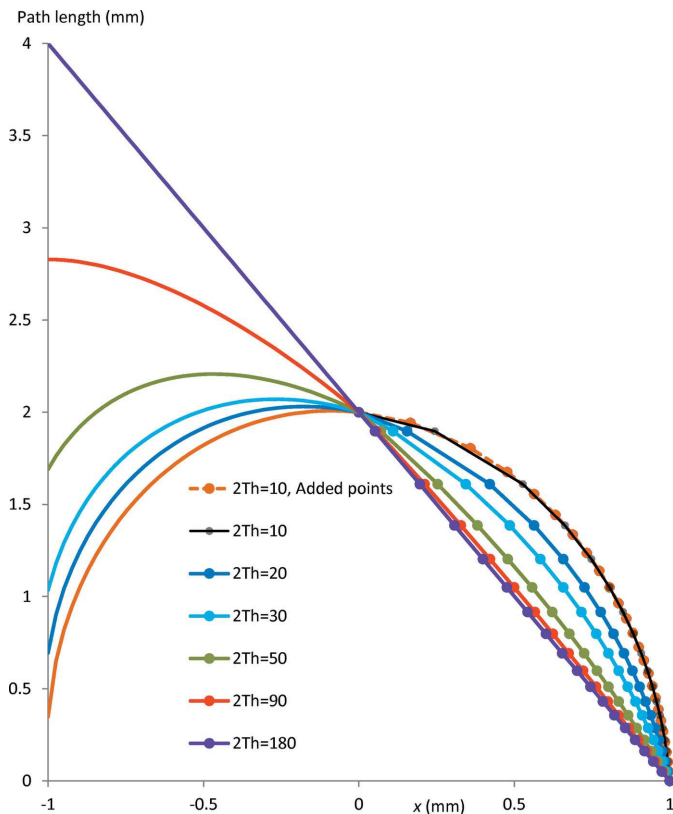
Figure 3
Path length through the disc as a function of x at $y = 0$ for various 2θ values. For the solid lines, the positions of the x_j values (the markers) were determined using equation (4) for $\mu = 20$ cm^{-1}. For the dashed line, corresponding to $10°$ 2θ, the x_j values were determined using equation (5).

Figure 4
x_j determined using equation (5) *versus* j for various 2θ and μ at $y = 0$ for $N_y = 40$ and $r = 1$ mm. μ values in cm^{-1} and 2θ values in $°$.

Fig. 5 shows a representation of $I(x, y)$ for all x and y within the disc for the cases of $N_y = 100$ and 40; the x_j positions can be seen as smeared dots. The smaller $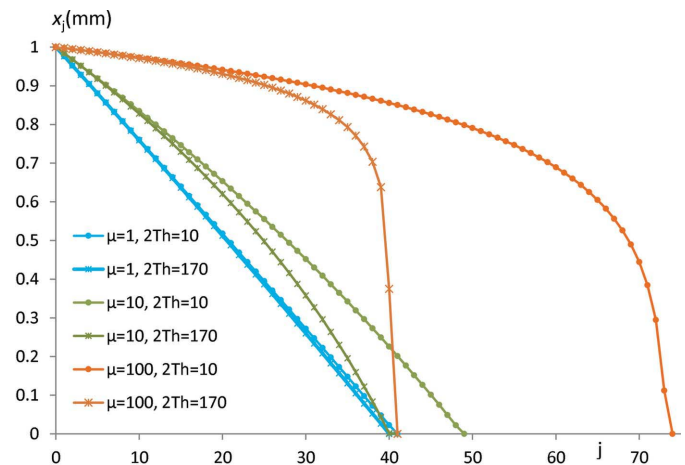N_y = 40$ case is computationally fast and produces accurate aberrations with regard to intensities, shapes and positions.

3. Creating a 2θ scan from the diffracting intensities on the disc

A diffraction pattern, $L(2\varphi)$, in the present context, comprises line segments connecting equally spaced points. The intensity contribution, $I(x_j, y)$, at the point (x_j, y) on the disc is detected at $2\varphi_d(x_j, y)$, where $2\varphi_d(x_j, y)$ is also a function of the focal length, R_f, and the specimen-to-detector distance, R_s. $I(x_j, y)$ is transformed to $L(2\varphi)$ by splitting $I(x_j, y)$ into two 2φ points, $2\varphi_1$ and $2\varphi_2$, corresponding to 2φ just before and just after $2\varphi_d$, respectively, as described by equation (6):

$$I(x_j, y)(2\varphi_2 - 2\varphi_d)/\Delta 2\varphi \quad \text{added to} \quad L(2\varphi_1),$$
$$I(x_j, y)(2\varphi_d - 2\varphi_1)/\Delta 2\varphi \quad \text{added to} \quad L(2\varphi_2), \quad (6)$$
$$\text{where} \quad \Delta 2\varphi = (2\varphi_2 - 2\varphi_1).$$

The two points, $L(2\varphi_1)$ and $L(2\varphi_2)$, of equation (6) have the same moment as $L(2\varphi_d)$ and the same intensity as the original intensity, or $L(2\varphi_d) = L(2\varphi_1) + L(2\varphi_2)$. The intensity and centroid of the aberration is therefore independent of the 2φ-axis position. For a single point, the integral breadth of equation (6) is equivalent to $\Delta 2\varphi$. This introduces a small amount of broadening in the final profile, which, in practice, is negligible and can only be observed, in a least-squares sense, if the observed profile is re-binned numerically at smaller step sizes than the original step size [equation (8), Coelho et al. (2015)]. For example, consider a line profile, L, comprising a single nonzero point. Fitting a delta function convoluted with two impulse functions to L, using TOPAS-Academic, results in the width of the impulse function refining to zero. Re-binning L at much smaller steps, $\Delta 2\varphi_{small}$, and again fitting a delta function with two impulse functions, results in the width of both impulse functions refining to a value equal to the original $\Delta 2\varphi$. Detection of the extra broadening introduced by equation (6) i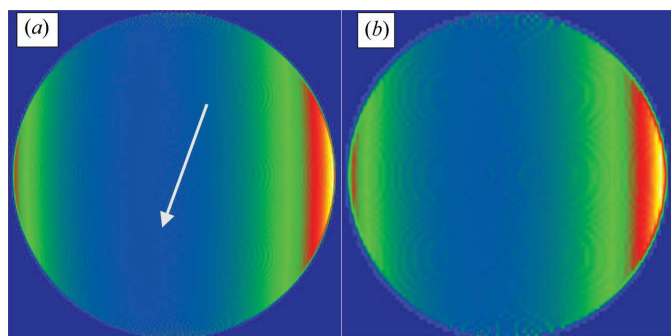s therefore not typically observed, as scan data are often re-binned at step sizes larger than the original step size and not at smaller step sizes.

Fig. 6 shows the aberration produced using equation (6) for a line through the disc at $y = 0$ for the defocused case of $R_f > R_s$ and for two $\Delta 2\varphi$ step sizes. The ripples at small $\Delta 2\varphi$ are due to the discrete nature of the process. Nevertheless, the aberration has the correct intensity and centroid moment. The ripples for $\Delta 2\varphi = 0.001°$ 2θ can be removed by convoluting three impulse functions of width H, as defined in equation (7), where $2\varphi(x_j, y)$ is the detected 2θ position of the ray diffracting from the (x_j, y) position on the disc:

$$H = \max\left[\left|2\varphi(x_{j+1}, y) - 2\varphi(x_j, y)\right|\right] \quad \text{for all } j. \quad (7)$$

The impulse functions are symmetric and normalized and hence do not change the intensity or centroid of $L(2\varphi)$. Fig. 7 shows aberrations from a line through the disc after applying the three smoothing impulse function convolutions with width H for various N_y and y values for $\Delta 2\varphi = 0.001°$ 2φ; as can be
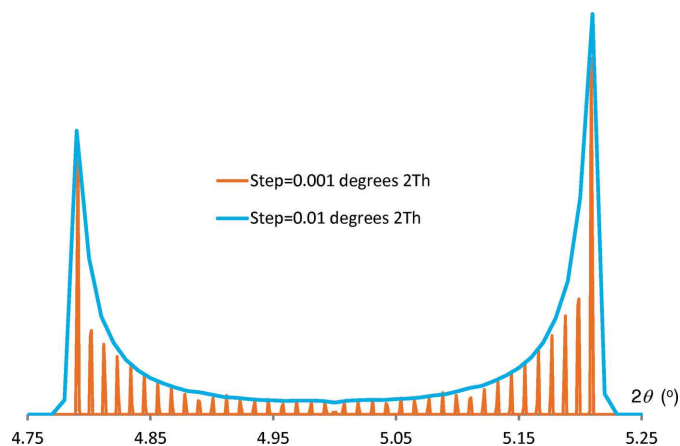
Figure 6
Convergent beam geometry aberration for a line-on-disc lying on the x axis at $y = 0$ for $N_y = 20$, with $\Delta 2\varphi = 0.01$ and $0.001°$ 2θ. $r = 1$ mm, $R_s = 200$ mm, $R_f = 800$ mm and $\mu = 20$ cm^{-1}.

Figure 5
$I(x, y)$ for $\mu = 15$ cm^{-1} and for $20°$ 2θ for (a) $N_y = 100$ and (b) $N_y = 40$. Red and yellow show areas of high intensity. The coordinate system is as outlined in Fig. 2. The arrow indicates the direction of the incident beam.
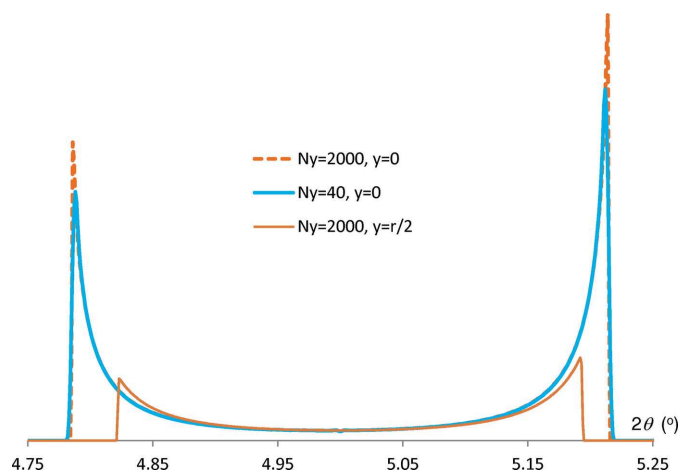

Figure 7
Convergent beam geometry aberrations for a line-on-disc parallel to the x axis for various N_y and y values for $\Delta 2\varphi = 0.001°$ 2θ. $r = 1$ mm, $R_s = 200$ mm, $R_f = 800$ mm and $\mu = 20$ cm^{-1}.

seen, the ripples have been smoothed and the aberration looks very similar to the aberration for $N_y = 2000$; the latter has a much smaller H applied.

4. Summing line-on-disc aberrations to form the final disc aberration

Summing N_y line aberrations with y values equally spaced from $-r$ to r produces the final aberration, but with bumps corresponding to the use of discrete y values. The final aberration can be smoothed by including the difference in 2φ between the line-on-disc aberrations. The enhanced H definition is given by

$$H = \max \left[\left| 2\varphi(x_{j+1}, y) - 2\varphi(x_j, y) \right|, \\ \left| 2\varphi(x = 0, y_{k+1}) - 2\varphi(x = 0, y_k) \right| \right] \quad \text{for all } j. \quad (8)$$

Fig. 8 shows the final aberration for a convergent and divergent beam with and without the application of the three impulse smoothing convolutions. As can be seen, the application of the convolutions for the $N_y = 40$ case produces an
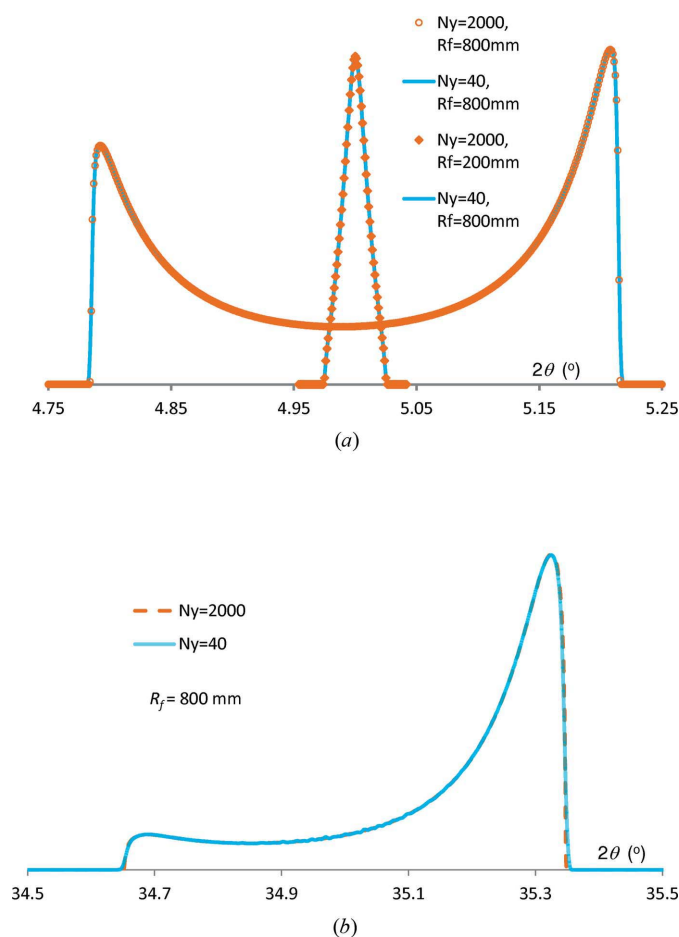
almost identical aberration to the $N_y = 2000$ case where the impulse convolutions were not applied.

For accurate integrated intensities at very low μ, $\mu < 0.1$ cm^{-1} depending on r, only two x_j points are needed per y line-on-disc ($x_{1,j} = 0$ and $x_{2,j} = r_y$). However, such a low number of points would not accurately describe the shape of the aberration in 2θ space; hence the use of equation (5) in determining $x_{.,j}$ values.

5. Comparison with ray tracing

The present disc aberration was compared with a ray-tracing approach (Appendix A) over the 2θ range of 5 to 175° for (a) convergent ($R_f = 200$ mm), (b) semi-convergent ($R_f = 800$ mm), (c) divergent ($R_f = 200$ mm) and (d) parallel incident beams for $R_s = 200$ mm, $r = 1$ mm and $\mu = 20$ cm^{-1}. The peak intensities, shapes and positions all closely agreed (see Fig. 14 in Appendix A).

6. Speed and approximating disc aberrations from nearby disc aberrations

For $N_y = 40$, present laptop computers can calculate ~20 000 disc aberrations per second; however, using the aberration buffer of *TOPAS-Academic*, no more than ~30 disc aberrations need be calculated for a particular geometry. The change in disc aberration shapes as a function of 2θ, as seen in Fig. 9, is smooth and can be considered linear over a small 2θ range. Aberrations at a particular 2θ can therefore be approximated from nearby calculated aberrations; this approximation is very accurate when the nearby calculated aberrations are no more than 2° 2θ apart, or the distance between calculated aberrations is limited to 4° 2θ. Equation (9) shows the formulation of the approximation:

Figure 8
(a) Convergent and (b) divergent beam geometry disc aberrations for various N_y and R_f obtained by summing line aberrations. $r = 1$ mm, $R_s = 200$ mm and $\mu = 20$ cm^{-1}. For $N_y = 40$, the smoothing impulse convolutions defined in equation (8) have been applied. They were not applied for $N_y = 2000$.
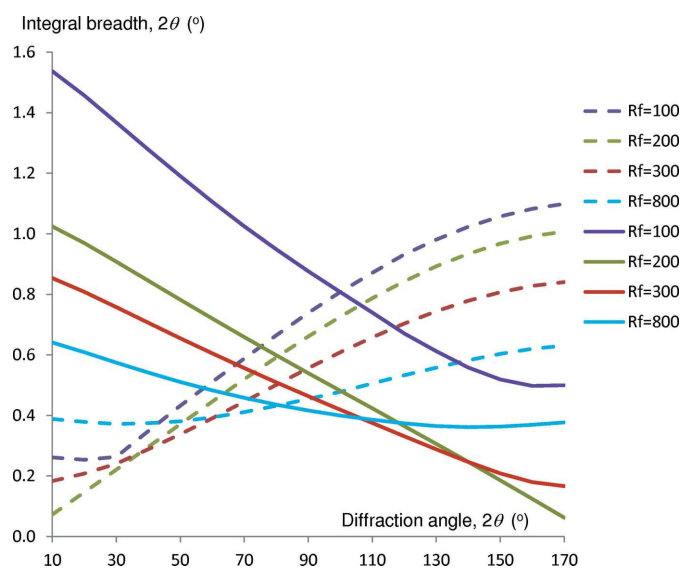

Figure 9
Integral breadths for convergent (dashed lines) and divergent (solid lines) beam geometries for disc aberrations as a function of 2θ and R_f. R_f values in mm. $r = 1$ mm, $R_s = 200$ mm and $\mu = 5$ cm^{-1}.

Table 1
(a) Convergent and (b) divergent beam geometry disc aberration statistics for $r = 1$ mm, $R_s = 200$ and $\Delta 2\varphi = 0.001°$ 2θ for 17 peaks in the range 10–170° 2θ for various focal lengths, R_f, and absorption coefficients, μ.

ΔCentroid and ΔI correspond to the centroid difference in degrees and the percentage difference in integrated intensity, respectively, between aberrations calculated with $N_y = 40$ and $N_y = 2000$. Min: minimum; Max: maximum; Stdev: standard deviation.

(a) Convergent beam geometry.

R_f (mm)		μ (cm⁻¹)				
		5	10	20	50	100
100	Min Centroid	−0.036462	−0.074507	−0.143973	−0.247643	−0.273500
	Max Centroid	−0.005513	−0.009507	−0.013640	−0.016972	−0.018181
	Min ΔCentroid	0.000002	0.000006	0.000007	−0.000018	−0.000026
	Max ΔCentroid	0.000011	0.000031	0.000072	0.000145	0.000055
	Stdev ΔCentroid	0.000003	0.000008	0.000022	0.000044	0.000023
200	Min Centroid	0.000065	0.000076	0.000100	0.000133	0.000149
	Max Centroid	0.000401	0.000484	0.000693	0.001035	0.001163
	Min ΔCentroid	0.000000	0.000000	0.000000	0.000000	0.000000
	Max ΔCentroid	0.000000	0.000000	0.000000	0.000000	0.000000
	Stdev ΔCentroid	0.000000	0.000000	0.000000	0.000000	0.000000
300	Min Centroid	0.001923	0.003271	0.004684	0.005846	0.006274
	Max Centroid	0.012694	0.025486	0.048916	0.083482	0.091891
	Min ΔCentroid	−0.000004	−0.000010	−0.000024	−0.000049	−0.000019
	Max ΔCentroid	−0.000001	−0.000002	−0.000002	0.000007	0.000009
	Stdev ΔCentroid	0.000001	0.000003	0.000008	0.000015	0.000008
800	Min Centroid	0.004245	0.007264	0.010417	0.012996	0.013942
	Max Centroid	0.028070	0.056785	0.109336	0.187165	0.206245
	Min ΔCentroid	−0.000009	−0.000023	−0.000055	−0.000109	−0.000042
	Max ΔCentroid	−0.000002	−0.000005	−0.000005	0.000015	0.000021
	Stdev ΔCentroid	0.000002	0.000006	0.000017	0.000034	0.000018

Convergent and divergent beam geometry intensity statistics for all R_f

		5	10	20	50	100
	Min % ΔI	0.022	−0.015	−0.115	−0.555	−1.136
	Max % ΔI	0.089	0.116	0.149	0.202	0.191
	Stdev % ΔI	0.021	0.040	0.076	0.182	0.314

(b) Divergent beam geometry.

R_f (mm)		μ (cm⁻¹)				
		5	10	20	50	100
100	Min Centroid	0.016763	0.028827	0.041434	0.051757	0.055547
	Max Centroid	0.111218	0.226219	0.436775	0.748723	0.825092
	Min ΔCentroid	−0.000036	−0.000095	−0.000220	−0.000438	−0.000166
	Max ΔCentroid	−0.000008	−0.000019	−0.000021	0.000060	0.000084
	Stdev ΔCentroid	0.000009	0.000024	0.000067	0.000135	0.000072
200	Min Centroid	0.011203	0.019243	0.027637	0.034498	0.037013
	Max Centroid	0.074238	0.150827	0.291003	0.498796	0.549773
	Min ΔCentroid	−0.000024	−0.000063	−0.000147	−0.000292	−0.000111
	Max ΔCentroid	−0.000005	−0.000013	−0.000014	0.000039	0.000055
	Stdev ΔCentroid	0.000006	0.000016	0.000045	0.000090	0.000048
300	Min Centroid	0.009348	0.016049	0.023042	0.028756	0.030850
	Max Centroid	0.061920	0.125727	0.242499	0.415610	0.458098
	Min ΔCentroid	−0.000020	−0.000052	−0.000122	−0.000243	−0.000092
	Max ΔCentroid	−0.000004	−0.000011	−0.000011	0.000033	0.000046
	Stdev ΔCentroid	0.000005	0.000013	0.000037	0.000075	0.000040
800	Min Centroid	0.007029	0.012056	0.017301	0.021587	0.023158
	Max Centroid	0.046529	0.094375	0.181930	0.311713	0.343572
	Min ΔCentroid	−0.000015	−0.000039	−0.000092	−0.000182	−0.000069
	Max ΔCentroid	−0.000003	−0.000008	−0.000008	0.000024	0.000034
	Stdev ΔCentroid	0.000004	0.000010	0.000028	0.000056	0.000030

$$A_2(\varepsilon_2) = A_1(\varepsilon_1)\alpha + A_3(\varepsilon_3)(1 - \alpha),$$
$$\text{where} \quad \varepsilon_n = 2\varphi - 2\theta_n \tag{9}$$
$$\text{and} \quad \alpha = (2\theta_3 - 2\theta_2)/(2\theta_3 - 2\theta_1).$$

Fig. 10 shows the very good approximation for $2\theta = 7°$ using aberrations calculated at 5 and 9°; this is an extreme case where $R_f \gg R_s$ and $2\theta_1$ is at the low angle of 5°. The use of the approximation of equation (9) results in ∼30 aberration calculations, even when hundreds of diffraction patterns each with thousands of peaks are synthesized, and is an important factor in speeding up large Rietveld refinements (Rietveld, 1969).

7. Preliminary analysis

Table 1 shows statistics obtained for convergent and divergent beam geometries for various R_f and μ for $N_y = 40$ compared to the same aberrations produced with $N_y = 2000$. These data represent a broad range of μr (0–10) and r/R_f values, demonstrating the accurate description of the present disc aberration. Aberrations with $\mu r > 10$ are also accurate because of the variable step size as determined by equation (5). Table 2 shows the small integral breadth variations between $N_y = 40$ and $N_y = 2000$; for accuracy, the aberrations for integral breadth calculations were carried out with a very small step size of $\Delta 2\varphi = 0.0001°$ 2θ. The case of $R_s = R_f$ corresponds to the worst-case scenario, as the focusing condition is maximized and the peaks are therefore at their sharpest at low angles. The case in Table 2 with a percentage difference greater than 1% occurs for the high-absorbing $\mu = 100$ cm⁻¹; at this high μ, the small diffraction volume results in a small integral breadth of 0.0133° 2θ. Fig. 9 shows the increase in broadening for both convergent and divergent beam geometries as $|R_f - R_s|$ increases; for convergent beam geometry, broadening increases with increasing 2θ, whereas for divergent beam geometry, broadening decreases with increasing 2θ. These trends can be understood by considering the case $\mu \rightarrow 0$, where from symmetry and the position of the focal point a disc aberration for convergent beam geometry at 2θ is the same as a disc aberration for divergent beam geometry at $180 - 2\theta$. Note that x_j points for low μ are similar for both high and low 2θ angles, as shown in Fig. 4.

Fig. 11 shows an $I(x, y)$ representation of the high-absorbing material LaB$_6$, where μ is set to the expected value for molybdenum $K\alpha$ radiation. The small diffraction region with appreciable intensity for the low angle of 20° 2θ, relative to the larger diffraction volume at 120° 2θ, is clear.

8. Analysis of LaB$_6$ data

LaB$_6$ powder, NIST SRM 660a (NIST, 2000), with a certified lattice parameter of 0.41569162 (97) nm at 295.7 K, was mounted in a capillary with an estimated

Table 2
Convergent beam geometry integral breadth (IB) calculations for $\Delta 2\varphi = 0.0001°\ 2\theta$ with $R_s = R_f = 200$ mm and $r = 1$ mm.

IB corresponds to the value obtained with $N_y = 2000$; ΔIB corresponds to the difference between integral breaths calculated at $N_y = 2000$ and $N_y = 40$.

| Bragg angle (° 2θ)	$\mu = 5$ cm^{-1}			$\mu = 100$ cm^{-1}		
	IB (° 2θ)	ΔIB (° 2θ)	ΔIB (%)	IB (° 2θ)	ΔIB (° 2θ)	ΔIB (%)
10	0.0728	0.0001	0.1175	0.0133	0.0004	3.1854
20	0.1467	−0.0002	−0.1098	0.0376	0.0003	0.7055
30	0.2209	0.0000	0.0028	0.0721	0.0005	0.6241
40	0.2960	−0.0001	−0.0288	0.1173	0.0004	0.3171
50	0.3710	0.0000	−0.0117	0.1721	0.0004	0.2225
60	0.4458	0.0000	−0.0026	0.2359	0.0004	0.1692
70	0.5196	0.0000	−0.0078	0.3078	0.0003	0.1063
80	0.5915	−0.0001	−0.0181	0.3866	0.0003	0.0885
90	0.6609	−0.0002	−0.0276	0.4713	0.0003	0.0709
100	0.7265	−0.0002	−0.0216	0.5601	0.0005	0.0956
110	0.7878	−0.0004	−0.0469	0.6519	0.0004	0.0676
120	0.8436	−0.0004	−0.0470	0.7444	0.0003	0.0422
130	0.8929	−0.0005	−0.0608	0.8356	0.0005	0.0605
140	0.9351	−0.0009	−0.0989	0.9229	0.0003	0.0295
150	0.9689	−0.0012	−0.1224	1.0026	−0.0008	−0.0751
160	0.9937	−0.0016	−0.1575	1.0705	−0.0015	−0.1412
170	1.0089	−0.0018	−0.1822	1.1199	−0.0043	−0.3857
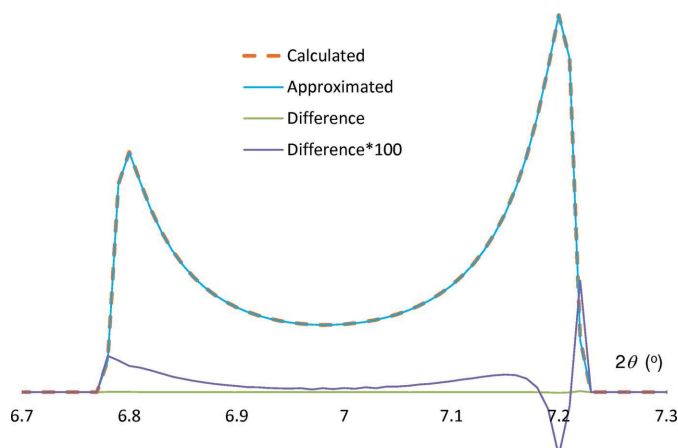
Figure 10
Convergent beam geometry disc aberration approximated at 7° 2θ compared with calculated aberration. The calculated aberration uses the method described in the paper. The approximated aberration uses equation (9) with the A_1 and A_3 aberrations calculated using the method described in the paper, one at 5° 2θ and one at 9° 2θ. $r = 1$ mm, $R_s = 200$ mm, $R_f = 800$ mm and $\mu = 20$ cm^{-1}.
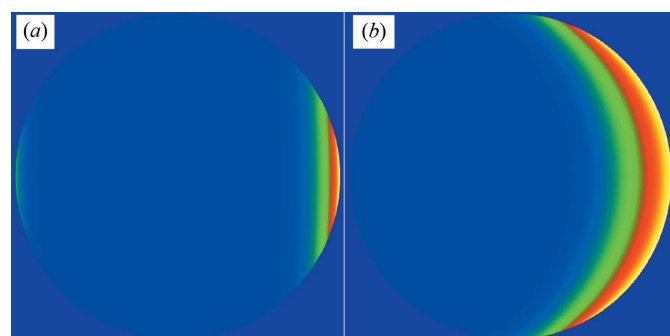

Figure 11
$I(x, y)$ for LaB$_6$ with $R_s = R_f = 200$ mm and $r = 0.5$ mm at (a) 20° 2θ and (b) 120° 2θ. $\mu = 58$ cm^{-1}, similar to what can be expected with molybdenum $K\alpha$ radiation with a packing density of 0.4.

diameter of 0.3–0.5 mm and scanned with Stoe and Bruker AXS D8 diffractometers equipped with a focusing Johannson-type Ge(220) monochromator and using molybdenum $K\alpha_1$ radiation. Scans were in the range 5–90° 2θ and 5–120° 2θ, respectively, and with step sizes in the data of 0.012 and 0.004° 2θ, respectively, with the diffractometers in convergent
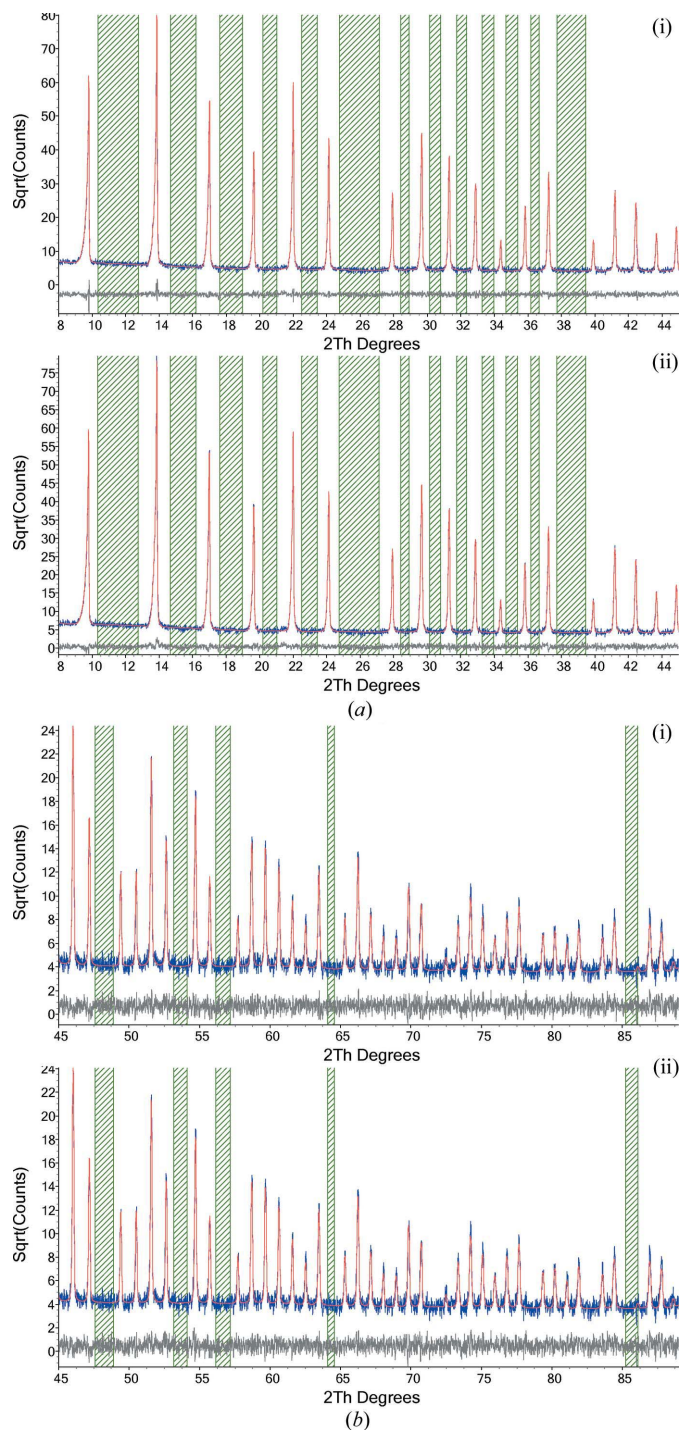

Figure 12
LaB$_6$ refinement fit for (a) low-angle and (b) high-angle Stoe diffractometer data, obtained (i) empirically using $\tan(\theta)$ Gaussian broadening and (ii) using the present disc convolution. Green thatched regions correspond to regions that have been excluded from the refinement.

Table 3
Convergent beam geometry LaB$_6$ refinement results for Stoe and Bruker AXS diffractometers for cases (1) and (3), obtained empirically using tan(θ) Gaussian broadening, and cases (2) and (4), using the present disc convolution.

Expected values are in bold. Underlined values were fixed and not refined. Equivalent temperature factors, $B_{eq} = 8\pi^2 U_{iso}$, in all cases were set to 0.5. The space group used was $Pm\bar{3}m$; fractional coordinates were not refined and were set to (0, 0, 0) for the La site and (0.19169, $\frac{1}{2}$, $\frac{1}{2}$) for the B site.

	Stoe		Bruker AXS D8	
	Case (1) Semi-empirical	Case (2) Disc convolution	Case (3) Semi-empirical	Case (4) Disc convolution
R_{wp}(%)	11.12	10.61	9.37	9.48
R_{Bragg} (%)	2.28	2.23	2.28	2.29
Soller slit angle (°)	4.29 (3)	4.30 (3)	2.818 (8)	2.842 (9)
Lattice parameter	4.15499 (9)	4.15663 (7)	4.15604 (7)	4.15618 (5)
Zero error (° 2θ)	−0.0045 (23)	−0.001 (2)	−0.0045 (23)	0.040 (1)
Perpendicular energy dispersive (mm)	−7.5 (3)	−0.43 (36)	−6.19 (13)	−5.81 (10)
Parallel energy dispersive (mm)	1.1 (0.5)	−0.37 (41)	−5.46 (28)	−5.54 (22)
Gaussian × tan(θ) (° 2θ)	0.1741 (8)	–	0.0941 (6)	–
Sabine intensity	1.42(2)	–	1.014 (10)	–
Focal length (mm)	–	198 (1), **217**	–	235 (1), **217**
Capillary diameter (mm)	–	0.5718 (1), **0.3–0.5**	–	0.350 (2), **0.3–0.5**
Packing density	–	0.312 (4), **0.3–0.6**	–	<u>0.4</u>

Refinement with perpendicular and parallel displacement parameters fixed and set to zero

R_{wp}(%)	11.92	11.43	10.62	10.72
Lattice parameter (Å)	4.15694 (2)	4.15674 (4)	4.156541 (8)	4.156543 (8)

Table 4
Percentage correlations obtained from the correlation matrix for LaB$_6$ refinement of data from Stoe and Bruker AXS D8 instruments [cases (2) and (4) of Table 3].

Percentage correlation of the a lattice parameter with 2θ shift parameters.

	Stoe	Bruker AXS D8
Zero error	49	89
Perpendicular displacement	56	72
Parallel displacement	44	90

beam geometry and the focus of the beam approximately at the detector, or $R_f = R_s$. The receiving slit width was 0.1 mm and Soller slits were placed in the diffracted beam. The data were Rietveld refined using *TOPAS-Academic* for two scenarios: (*a*) a semi-empirical approach applying Sabine *et al.* (1998) intensity corrections plus a Gaussian convolution that increases in width with tan(θ); and (*b*) the present capillary convolution (see Table 3). In both scenarios the perpendicular and parallel displacement of the diffractometer axis from the specimen axis was refined using the formulation of Scarlett *et al.* (2011). Regions of the diffraction pattern void of peaks were excluded from the refinement. The fits for both scenarios are good, with similar R_{wp} and R_{Bragg} values. The Gaussian broadening for the semi-empirical scenario, cases (1) and (3), is large; the Stoe diffractometer fit, case (1), has small peak position misfits on the low-angle 100 and 110 peaks at 9.8 and 13.8° 2θ, respectively, as shown in Fig. 12. These misfits are a result of there being too little broadening, which could be due to instrument misalignment factors. The D8 diffractometer is sharper with a smaller Soller acceptance angle and a smaller capillary diameter. The larger than expected parallel and perpendicular displacements for cases (1), (3) and (4) are probably due to the high correlations between the a lattice

parameter and the 2θ shift parameters, as seen in Table 4. These high correlations emphasize the need for careful instrument alignment with the displacement parameters fixed to zero and not refined. Doing so on these data, except for case (2), produces the significantly larger R_{wp} values seen at the bottom of Table 4. It is worth noting that negligible peak shifts are expected for this instrument and specimen configuration, where μ is expected to be ~60 cm^{-1} and the focal length is expected to be similar to the diffractometer radius; from Table 1(*a*) the expected maximum centroid shift for r = 1 mm is <0.001° 2θ; for r < 1 mm the expected shift should be even less.

Except for the large displacement parameters of case (4), the present disc convolution fits the whole 2θ range with parameters that are physically reasonable, as seen in Table 3, cases (2) and (4), and Fig. 12. The linear absorption coefficient used was that calculated for LaB$_6$ and then multiplied by a refinable packing density parameter; this parameter refined to a reasonable value of 0.31. The focal length, R_f, refined to 198 and 235 mm; this is not far off the perfectly focused beam of 217 mm. The diameter of the capillary refined to reasonable values of 0.57 and 0.35 mm. Fixing, and not refining, capillary diameters to accurate measured values would reduce correlations and improve robustness in the fitting process.

9. Discussion

The accuracy of the disc convolution presented here can be broken down into two parts; the intensity accuracy and the peak shape/position accuracy. The intensity accuracy is governed by the number of data points sampled across the disc, which is dependent on the chosen value for N_y. For a very small μ, the intensity can be accurate using a small N_y. Too small a value of N_y, however, leads to inaccurate peak shapes and positions. For a sufficiently large N_y, equation (5) solves these problems, concentrating points in parts of the disc that contribute to intensity. N_y = 40 results in very accurate aberrations with regard to intensity, shape and position, as shown in Tables 1 and 2. This accuracy has been measured against the disc aberration itself and does not include additional broadening as would be experienced with real observed data originating from the source emission profile, and instrument and specimen broadening. It is therefore probable that the extreme accuracy obtained with N_y = 40 is not warranted in most situations. However, the speed at which the disc aberration can be calculated is small in comparison to other

calculations necessary in synthesizing line profiles, and hence reduction in N_y is not warranted.

10. Conclusion

A fast and accurate numerical approach to calculating aberrations originating from a capillary in the equatorial plane, a disc, has been developed for convergent, divergent and parallel beam instrument geometries. The aberration is then convoluted with an emission profile and instrument and specimen aberrations to form a diffraction pattern, which is used in Rietveld refinement. Refinement of the fundamental parameters of the capillary diameter, the focal length and the specimen linear absorption coefficient should agree with expected or measured values.

APPENDIX *A*
A1. Validation of model, ray tracing

A ray-tracing model was constructed to simulate the effect of convergent, divergent and parallel monochromatic incident X-ray beams of uniform intensity on the resultant aberration peak shapes, positions and intensities. In this model (Fig. 13), the X-ray beam is incident on the disc from left to right, along the x axis, and completely bathes the disc. There are N points, O', distributed evenly throughout the disc. Each ray enters and exits the disc at R and R', diffracting at O' through an angle 2θ, and is detected at D, at an angle 2φ. The focal length and specimen-to-detector distance are given by R_f and R_s, respectively. The total path length through the disc, P, is given by $P_p + P_s$. To form a ray-tracing aberration, N points were generated in polar coordinates

$$(\rho, \kappa) = (r U_1^{1/2}, 360 U_2), \tag{10}$$

where U is a random number uniformly distributed in the range [0, 1]. The square root ensures that each point has an equal area associated with it. The calculation of the angle α allows for the easy conversion of the model between convergent, divergent and parallel incident X-ray beams. α is given by
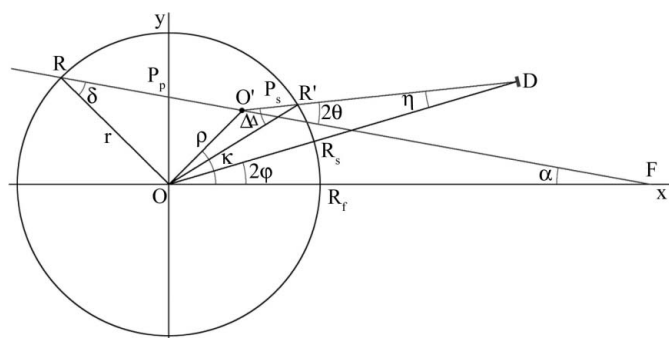
$$\alpha = G \arctan\left[\frac{\rho \sin(\kappa)}{R_f - G\rho \cos(\kappa)}\right], \tag{11}$$

where G denotes the instrument geometry; 1 is convergent, -1 is divergent and 0 is parallel. The path length can then be calculated by

$$\delta = \arcsin\left[\frac{\rho \sin(\kappa + \alpha)}{r}\right], \tag{12}$$

$$\Delta = \arcsin\left[\frac{\rho \sin(\kappa + \alpha - 2\theta)}{r}\right], \tag{13}$$
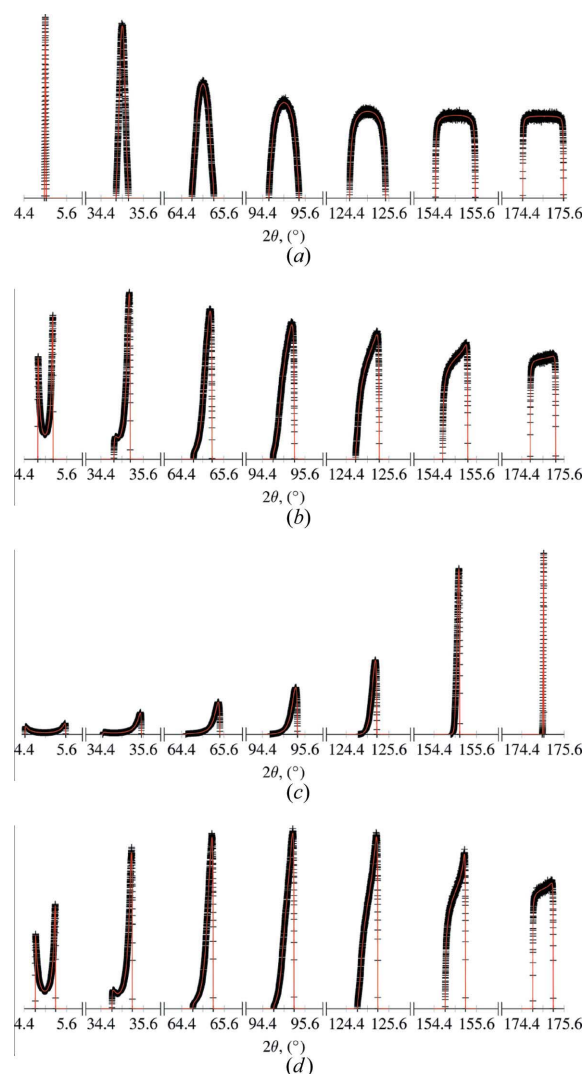
Figure 14
Ray-tracing and aberration model fits for (*a*) convergent ($R_f = 200$ mm, $R_p = 1.33\%$), (*b*) semi-convergent ($R_f = 800$ mm, $R_p = 1.07\%$), (*c*) divergent ($R_f = 200$ mm, $R_p = 0.835\%$) and (*d*) parallel ($R_p = 0.989\%$) incident beams. The ray-tracing data were calculated for $R_s = 200$ mm, $r = 1$ mm, $\mu = 20$ cm^{-1}, $N = 20 \times 10^6$ and $\varepsilon_\Delta = 0.0005°$. Only a subset of the peaks are shown for clarity. All data within each section are displayed on a common vertical axis, except for the first peak in (*a*), where the vertical axis is compressed by a factor of 6, and the last peak in (*c*), where the factor is 4.5.

Figure 13
Ray-trace geometry. A ray, focused at F, enters and exits the disc at R and R', diffracting at O' through an angle 2θ, and is detected at D at an angle 2φ, having travelled through the disc with a total path length of $P_p + P_s$.

$$P = P_p + P_s = \rho \left[\frac{\sin(\kappa + \alpha + \delta)}{\sin(\delta)} + \frac{\sin(\kappa + \alpha - \Delta - 2\theta)}{\sin(\Delta)} \right],$$

(14)

where 2θ is the diffraction angle taken with respect to the incident ray. The relative transmitted intensity can then be calculated as

$$t = \exp(-\mu P), \tag{15}$$

where μ is the linear absorption coefficient of the diffracting material. The diffracted ray is detected at 2φ, where this angle is taken with respect to the centre of the goniometer. The deviation of the diffracted beam from its expected position, $\varepsilon = 2\varphi - 2\theta$, can be calculated by

$$\eta = \rho \sin\left(\frac{\kappa + \alpha - 2\theta}{R_s} \right), \tag{16}$$

$$\varepsilon = \eta - \alpha. \tag{17}$$

These equations allow for a complete mapping of $(\rho, \kappa) \rightarrow (2\varphi, t)$. To calculate the entire diffraction peak shape and intensity, centred 2φ bins of width ε_Δ were created and a total relative transmitted intensity for each bin was calculated as

$$T = \frac{\sum t}{N \varepsilon_\Delta}, \tag{18}$$

where the sum was taken over all values of t for which the corresponding value of 2φ falls in that particular bin.

A2. Comparison with disc aberration

A total of 20×10^6 points were evenly distributed randomly throughout the disc, and the relative transmitted intensity, $\exp(-\mu P)$, and 2φ were calculated for each point. The relative transmitted intensities were then placed into centred 2φ bins

of width $0.0005°$, giving the total relative diffracted intensity for a given diffraction angle, 2θ. Diffraction peaks were generated every $5°$ from 5 to $175°$ 2θ. Numerous combinations of R_s, R_f, r and μ were tested. Examples of (a) convergent ($R_f = 200$ mm), (b) semi-convergent ($R_f = 800$ mm), (c) divergent ($R_f = 200$ mm) and (d) parallel incident beams for $R_s = 200$ mm, $r = 1$ mm and $\mu = 20$ cm^{-1} are shown in Fig. 14. The profile R factors,

$$R_p = \left(\frac{\sum_m |Y_{o,m} - Y_{c,m}|}{\sum_m Y_{o,m}} \right)^{1/2}, \tag{19}$$

for the various fits are given in the figure caption. Y_o are the observed intensities, and Y_c are the calculated intensities.

References

Cheary, R. W. & Coelho, A. A. (1998). *J. Appl. Cryst.* **31**, 851–861.
Coelho, A. A. (2017). *TOPAS-Academic V7*, http://www.topas-academic.net/.
Coelho, A. A., Chater, P. A. & Kern, A. (2015). *J. Appl. Cryst.* **48**, 869–875.
Dwiggins, C. W. (1972). *Acta Cryst.* A**28**, 219–220.
Dwiggins, C. W. (1975). *Acta Cryst.* A**31**, 146–148.
NIST (2000). SRM 660a. National Institute of Standards and Technology, US Department of Commerce, Gaithersburg, MD, USA.
Rietveld, H. M. (1969). *J. Appl. Cryst.* **2**, 65–71.
Sabine, T. M., Hunter, B. A., Sabine, W. R. & Ball, C. J. (1998). *J. Appl. Cryst.* **31**, 47–51.
Scarlett, N. V. Y., Rowles, M. R., Wallwork, K. S. & Madsen, I. C. (2011). *J. Appl. Cryst.* **44**, 60–64.
Sulyanov, S., Gogin, A. & Boysen, H. (2012). *J. Appl. Cryst.* **45**, 93–97.